

# A dust–parallax distance of 19 megaparsecs to the supermassive black hole in NGC 4151

Sebastian F. Hönig<sup>1,2</sup>, Darach Watson<sup>1</sup>, Makoto Kishimoto<sup>3</sup> & Jens Hjorth<sup>1</sup>

The active galaxy NGC 4151 has a crucial role as one of only two active galactic nuclei for which black hole mass measurements based on emission line reverberation mapping can be calibrated against other dynamical techniques<sup>1–3</sup>. Unfortunately, effective calibration requires accurate knowledge of the distance to NGC 4151, which is not at present available<sup>4</sup>. Recently reported distances range from 4 to 29 megaparsecs<sup>5–7</sup>. Strong peculiar motions make a redshift-based distance very uncertain, and the geometry of the galaxy and its nucleus prohibit accurate measurements using other techniques. Here we report a dust–parallax distance to NGC 4151 of  $19.0_{-2.6}^{+2.4}$  megaparsecs. The measurement is based on an adaptation of a geometric method that uses the emission line regions of active galaxies<sup>8</sup>. Because these regions are too small to be imaged with present technology, we use instead the ratio of the physical and angular sizes of the more extended hot-dust emission<sup>9</sup> as determined from time delays<sup>10</sup> and infrared interferometry<sup>11–14</sup>. This distance leads to an approximately 1.4-fold increase in the dynamical black hole mass, implying a corresponding correction to emission line reverberation masses of black holes if they are calibrated against the two objects with additional dynamical masses.

The central black hole in an active galactic nucleus (AGN) is surrounded by a putative accretion disk that emits predominantly in ultraviolet and optical wavelengths. At large distances from this central emission source, the gas is cool enough for dust to survive (temperature  $\lesssim 1,500$  K). This ‘dusty torus’ absorbs the ultraviolet–optical radiation and thermally reemits the energy in the infrared. Thus, any variability in the ultraviolet–optical emission will be detected in the dust emission with some time delay. Near-infrared reverberation mapping measures the time lag,  $\tau$ , between the ultraviolet–optical variability and the corresponding changes in emission of the hot dust. The hottest dust is located at about the sublimation radius,  $R_{\text{sub}} = R(T \approx 1,500 \text{ K})$ . The time lag can be converted into a physical size using  $R_{\tau} = \tau c$ , where  $c$  is the speed of light. Typically, time lags are in the range of several tens to hundreds of days, which corresponds to physical sizes of the order of 0.1 pc, with a square-root dependence on luminosity<sup>12,15</sup>.

In parallel, infrared interferometry at the same wavelength measures the angular size,  $\rho$ , of the same emission region. The angular and physical sizes are trigonometrically related by  $\sin(\rho) = R_{\tau}/D_A$ , where  $D_A$  is the angular-diameter distance to the object. For small angles,  $\sin(\rho) \approx \rho$  and, accounting for cosmological time dilation, we obtain  $D_A(\text{Mpc}) = 0.173\tau(\text{days})/(\rho(\text{mas})(1+z))$ , which forms the basis of the distance measurement presented here (Fig. 1). A geometric technique was first proposed for broad emission lines<sup>8</sup>. Unfortunately, the typical angular size of the broad-emission regions of bright AGNs is of the order of 0.001–0.01 mas, which is too small to be spatially resolved with today’s optical long-baseline interferometers. The dust continuum emission, however, is larger by a factor of  $\sim 4$ , and infrared interferometers have now managed to resolve about a dozen AGNs<sup>11,12,14,16</sup>. Moreover, using dust emission requires only photometric reverberation mapping instead of the spectral resolution of emission lines. Finally, dust physics is arguably easier to model than gas line emission.

To determine the distance to the supermassive black hole in NGC 4151, we make use of interferometry obtained with the two Keck telescopes and monitoring data from the literature. V-(wavelength  $0.55 \mu\text{m}$ ) and K-band ( $2.2 \mu\text{m}$ ) photometric monitoring from 2001 to 2006<sup>10</sup> traces the ultraviolet–optical and hot-dust emission, respectively. Because long-term brightness changes can cause  $\tau$  and  $\rho$  to increase or decrease, monitoring and interferometry data should be recorded more or less contemporaneously. We use six Keck interferometry measurements made between 2003 and 2010<sup>11–14</sup>. These overlap with the monitoring data, and inspection of long-term brightness trends showed that fluctuations were moderate between 2000 and 2010<sup>16</sup>. Indeed, no significant change in size has been detected for this set of interferometry and variability data<sup>16,17</sup>.

When comparing angular and physical sizes, it is important to make sure that they refer to the same physical region. First, observations of the dust emission are preferably made at the same waveband (here the K band). Second, the spatial distribution of the dust around the AGN affects the observed sizes (Fig. 1): dust that is homogeneously distributed will result in a larger apparent size than will a compact dusty region,

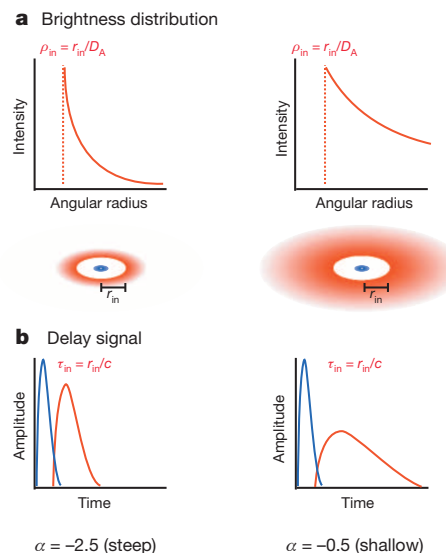


**Figure 1 | Effect of the brightness distribution on the observed sizes and time lags.** The bottom row (b) illustrates effects on the time lag signal of varying the brightness distribution (blue, optical; red, near-infrared), and the upper row (a) outlines the corresponding (interferometric) brightness distribution in the near-infrared. Compact distributions lead to shorter time lags and smaller interferometric radii than do shallow profiles. This information is encoded in the shape (width, amplitude) of the light curve. With a simple power-law parameterization, this smearing effect can be accounted for to determine the time lag and angular size of the innermost radius of the brightness distribution. The simultaneous modelling of light curves and interferometry results in a very precise angular distance measurement.

<sup>1</sup>Dark Cosmology Centre, Niels Bohr Institute, University of Copenhagen, Juliane Maries Vej 30, 2100 Copenhagen Ø, Denmark. <sup>2</sup>School of Physics & Astronomy, University of Southampton, Southampton SO17 1BJ, UK. <sup>3</sup>Department of Physics, Faculty of Science, Kyoto Sangyo University, Kamigamo-motoyama, Kita-ku, Kyoto 603-8555, Japan.

because for the former a larger region contributes to the emission at a given wavelength. As a consequence, the variability signal in the  $K$  band will show some degree of smoothing with respect to the  $V$  band signal, depending on the distribution. This also involves a shift of the peak time lag. At the same time, the size measured by interferometry will appear correspondingly smaller or larger. This distribution effect in both types of data can be effectively modelled by means of a disk model<sup>17,18</sup>, assuming that the dust is heated by AGN radiation and the projected brightness distribution is represented by the power law  $S(r) \propto r^\alpha$  (Methods). This geometry is in line with theoretical expectations and observational evidence of the hot-dust region<sup>19,20</sup>. Indeed, the model has been successfully applied to reproduce multiwavelength, multi-baseline interferometry of several AGNs<sup>14,21</sup> (including NGC 4151), as well as the light curve of NGC 4151<sup>17,22</sup>.

The common reference size in such a model is the inner radius,  $r_{\text{in}}$ , of the brightness distribution. For reverberation mapping and interferometry, this corresponds to a reference time lag  $\tau_{\text{in}} = r_{\text{in}}/c$  and angular size  $\rho_{\text{in}} \approx r_{\text{in}}/D_A$  of the inner boundary of the brightness distribution. Other parameters that may influence the observationally inferred physical and angular size of  $r_{\text{in}}$  are the disk geometry of the emission region and the dust properties. For the inclination and disk orientation, we use observational constraints based on the dynamics of the emission line region in NGC 4151 and polarimetry<sup>23–25</sup>. We do not consider the radio jet in this study<sup>26</sup>, because the available data do not allow both position angle and inclination to be reliably established at the same time. The absorption efficiency of the dust is implicitly included in our parameterization of the brightness distribution. Moreover, the sublimation temperature does not affect the distance determination because it scales in the same way for the reference angular sizes and the reference time lags (Methods).

Because the light curves are sampled with finite and varying gaps between the observations, we simulated 1,250 random, continuous representations of the data using the AGN variability pattern derived from the structure function. We calculated  $\tau_{\text{in}}$ ,  $\alpha$  and  $\rho_{\text{in}}$  simultaneously, given the observationally constrained inclination and disk orientation as priors. This resulted in 1,250 estimates of  $D_A$ , which are shown in Fig. 2. An important feature of this process is that, although determining the reference time lag or the reference angular size individually is quite uncertain, both parameters are strongly correlated with the dust brightness distribution. Thus, the ratio, that is,  $D_A$ , can be constrained with much higher precision than can the reference time lag or reference angular size individually, if  $\tau_{\text{in}}$  and  $\rho_{\text{in}}$  are calculated simultaneously given the inferred  $\alpha$ .

We obtain an angular-diameter distance to NGC 4151 of  $D_A = 19.0^{+2.4}_{-2.6}$  Mpc (Fig. 2, inset probability distribution). The error bars include statistical uncertainties from the reverberation and interferometric observations, as well as the systematic uncertainties introduced by the geometry, the brightness distribution and the uncertainty in the contributions of the host and the putative accretion disk to the  $K$ -band interferometry. These uncertainties have been accounted for in Monte Carlo simulations when sampling the data (Methods). The new distance clarifies the situation for NGC 4151. The galaxy is in the vicinity of the Virgo cluster ( $<30^\circ$  angular separation from the Virgo cluster centre), resulting in strong peculiar motion with respect to the Hubble flow<sup>6,27</sup>. Therefore, any recession-velocity-dependent distance has to be considered uncertain. Geometric megamaser distances require that the nuclear region is seen very close to edge-on, which is generally not the case for unobscured AGN. Moreover, a direct distance estimate based on the Tully–Fisher relation is difficult because of the face-on view of the galactic disk, which makes it difficult to determine the required rotational velocities. Attempts to estimate the distance this way resulted in a wide range of values between  $\sim 4$  and 20 Mpc (refs 5, 6). More recently, a luminosity distance of  $29.2 \pm 0.5$  Mpc was suggested on the basis of near-infrared reverberation mapping only and a model for the absorption and re-emission of dust, but cannot be reconciled with our new result or the other estimates<sup>7</sup>.

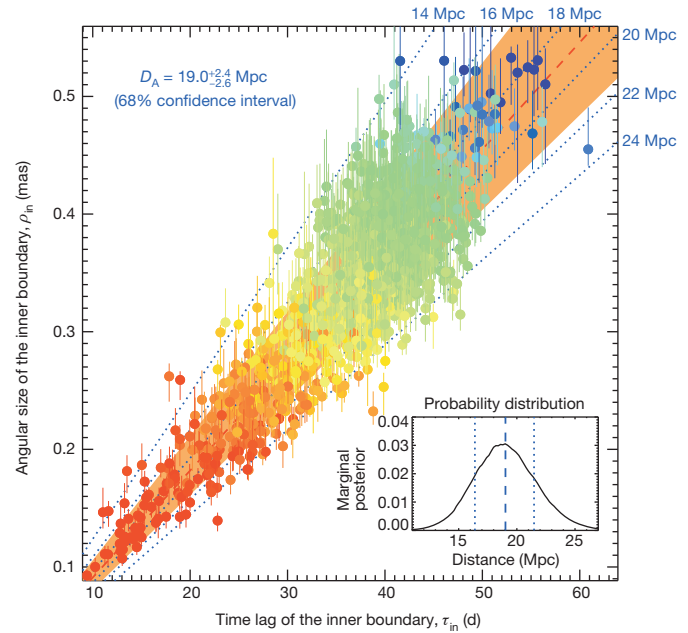


**Figure 2 | Relating time lags and angular sizes to measure the absolute distance to NGC 4151.** The coloured circles show the modelled reference time lags,  $\tau_{\text{in}}$ , and associated angular sizes,  $\rho_{\text{in}}$  (1,250 random realizations of the  $V$ -band light curve; 68% confidence interval shown as error bars). The dotted blue lines mark  $\tau_{\text{in}}/\rho_{\text{in}}$  ratios corresponding to distances in the range  $D_A = 14$ –24 Mpc. The distribution median and 68% confidence interval are marked by the dashed red line and the orange shaded area. Points are colour-coded to indicate the brightness distribution power-law index  $\alpha$ , in the range  $\alpha = 2$  (red; shallow) to  $\alpha = -15$  (blue; steep). Inset, probability distribution function of the inferred distance, with mean and 68% confidence interval indicated by the dashed and dotted lines, respectively.

The new precise distance to NGC 4151 is relevant because this galaxy is a cornerstone in calibrating black hole masses inferred by different methods<sup>2</sup>; apart from NGC 3227, it is the only galaxy with a suitable mass estimated from reverberation mapping, stellar and gas dynamics. Of both galaxies, NGC 4151 has much better mass constraints<sup>2</sup>, such that any systematic offset in distance will almost equally affect the calibration of black hole masses. Dynamical mass estimates relate the rotational velocity field of stars or gas surrounding the black hole to their distances from the AGN. In the process, observed angular distances have to be converted into physical distances, which requires knowledge of the absolute distance to the galaxy. The most recent mass estimates assume that  $D_A = 13.2$  Mpc (refs 4, 28). A stellar-velocity-based mass was reported as  $M_{\text{BH}}^{\text{SD}} = (3.76 \pm 1.15) \times 10^7 M_\odot$  (ref. 4), where  $M_\odot$  is the solar mass. Our new measurement implies that this mass is underestimated by a factor of  $\sim 1.4$ , leading to a revised mass of  $M_{\text{BH}}^{\text{SD}} = (5.4 \pm 1.8) \times 10^7 M_\odot$ . Similarly, the correction to the distance increases the gas dynamical mass<sup>28</sup> from  $M_{\text{BH}}^{\text{GD}} = 3.0^{+0.75}_{-2.2} \times 10^7 M_\odot$  to  $M_{\text{BH}}^{\text{GD}} = 4.3^{+1.2}_{-3.2} \times 10^7 M_\odot$ .

The new distance and the corrected values of  $M_{\text{BH}}^{\text{SD}}$  and  $M_{\text{BH}}^{\text{GD}}$  also affect the correction factor  $f$  that has to be invoked when converting reverberation time lags and velocities into black hole masses. The most recent reference value is  $f = 4.31 \pm 1.05$ , inferred from comparing reverberation mapping masses with black hole masses determined from the established relation between black hole mass  $M_{\text{BH}}$  and bulge stellar velocity dispersion  $\sigma_*$  (ref. 29). By using our corrected values for the dynamical black hole masses to calibrate the reverberation data<sup>1</sup>, we find a range of  $f = 5.2$ –6.5 (reflecting the difference between gas and stellar dynamical masses), implying a systematic shift to larger masses. Such larger  $f$  values may be generally applicable, as also suggested by complex modelling of velocity-resolved reverberation mapping data<sup>30</sup>.

**Online Content** Methods, along with any additional Extended Data display items and Source Data, are available in the online version of the paper; references unique to these sections appear only in the online paper.

**Received 26 June; accepted 3 October 2014.**

- Bentz, M. C. *et al.* A reverberation-based mass for the central black hole in NGC 4151. *Astrophys. J.* **651**, 775–781 (2006).
- Peterson, B. M. Measuring the mass of supermassive black holes. *Space Sci. Rev.* **183**, 253–275 (2014).
- Woo, J.-H. *et al.* Do quiescent and active galaxies have different  $M_{BH} - \sigma_*$  relations? *Astrophys. J.* **772**, 49 (2013).
- Onken, C. A. *et al.* The black hole mass of NGC 4151. II. Stellar dynamical measurement from near-infrared integral field spectroscopy. *Astrophys. J.* **791**, 37 (2014).
- Theureau, G. *et al.* Kinematics of the local universe. XIII. 21-cm line measurements of 452 galaxies with the Nançay radiotelescope. JHK Tully-Fisher relation, and preliminary maps of the peculiar velocity field. *Astron. Astrophys.* **465**, 71–85 (2007).
- NASA/IPAC Extragalactic Database, <http://ned.ipac.caltech.edu> (2014).
- Yoshii, Y. *et al.* A new method for measuring extragalactic distances. *Astrophys. J.* **784**, L11 (2014).
- Elvis, M. & Karovska, M. Quasar parallax: a method for determining direct geometrical distances to quasars. *Astrophys. J.* **581**, L67 (2002).
- Hönig, S. F. Dust reverberation mapping in the era of big optical surveys and its cosmological application. *Astrophys. J.* **784**, L4 (2014).
- Koshida, S. *et al.* Variation of inner radius of dust torus in NGC4151. *Astrophys. J.* **700**, L109 (2009).
- Swain, M. *et al.* Interferometer observations of subparsec-scale infrared emission in the nucleus of NGC 4151. *Astrophys. J.* **596**, L163 (2003).
- Kishimoto, M. *et al.* Exploring the inner region of type 1 AGNs with the Keck interferometer. *Astron. Astrophys.* **507**, L57–L60 (2009).
- Pott, J.-U. *et al.* Luminosity-variation independent location of the circumnuclear hot dust in NGC 4151. *Astrophys. J.* **715**, 736–742 (2010).
- Kishimoto, M. *et al.* The innermost dusty structure in active galactic nuclei as probed by the Keck interferometer. *Astron. Astrophys.* **527**, A121 (2011).
- Suganuma, M. *et al.* Reverberation measurements of the inner radius of the dust torus in nearby Seyfert 1 galaxies. *Astrophys. J.* **639**, 46–63 (2006).
- Kishimoto, M. *et al.* Evidence for a receding dust sublimation region around a supermassive black hole. *Astrophys. J.* **775**, L36 (2013).
- Hönig, S. F. & Kishimoto, M. Constraining properties of dusty environments by infrared variability. *Astron. Astrophys.* **534**, A121 (2011).
- Kishimoto, M. *et al.* Mapping the radial structure of AGN tori. *Astron. Astrophys.* **536**, A78 (2011).
- Kawaguchi, T. & Mori, M. Near-infrared reverberation by dusty clumpy tori in active galactic nuclei. *Astrophys. J.* **737**, 105 (2011).
- Landt, H. *et al.* The near-infrared broad emission line region of active galactic nuclei - II. The 1- $\mu$ m continuum. *Mon. Not. R. Astron. Soc.* **414**, 218–240 (2011).
- Hönig, S. F. *et al.* Dust in the polar region as a major contributor to the infrared emission of active galactic nuclei. *Astrophys. J.* **771**, 87 (2013).
- Schnülle, K. *et al.* Dust physics in the nucleus of NGC 4151. *Astron. Astrophys.* **557**, L13 (2013).
- Müller-Sánchez, F. *et al.* Outflows from active galactic nuclei: kinematics of the narrowline and coronal-line regions in Seyfert galaxies. *Astrophys. J.* **739**, 69 (2011).
- Das, V. *et al.* Mapping the kinematics of the narrow-line region in the Seyfert galaxy NGC 4151. *Astron. J.* **130**, 945–956 (2005).
- Martel, A. R. & New, H. Spectropolarimetry of NGC 4151: The broad-line region-host connection. *Astrophys. J.* **508**, 657–663 (1998).
- Mundell, C. G. The nuclear regions of the Seyfert galaxy NGC 4151: parsec-scale H I absorption and a remarkable radio jet. *Astrophys. J.* **583**, 192–204 (2003).
- Mould, J. R. *et al.* The Hubble Space Telescope Key Project on the Extragalactic Distance Scale. XXVIII. Combining the constraints on the Hubble constant. *Astrophys. J.* **529**, 786–794 (2000).
- Hicks, E. K. S. & Malkan, M. A. Circumnuclear gas in Seyfert 1 galaxies: morphology, kinematics, and direct measurement of black hole masses. *Astrophys. J. Suppl. Ser.* **174**, 31–73 (2008).
- Grier, C. J. *et al.* Stellar velocity dispersion measurement in high-luminosity quasar hosts and implications for the AGN black hole mass scale. *Astrophys. J.* **773**, 90 (2013).
- Pancoast, A. *et al.* The Lick AGN Monitoring Project 2011: dynamical modeling of the broad-line region in Mrk 50. *Astrophys. J.* **754**, 49 (2012).

**Acknowledgements** We thank R. Wojtak for discussions on peculiar velocities near the Virgo cluster. S.F.H. acknowledges support from the Marie Curie International Incoming Fellowship within the Seventh European Community Framework Programme (PIIF-GA-2013-623804). The Dark Cosmology Centre is funded by the Danish National Research Foundation. This research has made use of the NASA/IPAC Extragalactic Database (NED) which is operated by JPL, Caltech, under contract with NASA.

**Author Contributions** S.F.H. and D.W. had the idea for the project. S.F.H. collected the data, developed the model and wrote the paper. D.W. assisted in interpreting the results and helped to write the manuscript. M.K. contributed the interferometry data and helped with the data analysis. J.H. contributed to the modelling and interpretation. All authors engaged in discussion and provided comments on the manuscript.

**Author Information** Reprints and permissions information is available at [www.nature.com/reprints](http://www.nature.com/reprints). The authors declare no competing financial interests. Readers are welcome to comment on the online version of the paper. Correspondence and requests for materials should be addressed to S.F.H. ([s.hoenig@soton.ac.uk](mailto:s.hoenig@soton.ac.uk)).

## METHODS

**Principle of the measurement.** The present study makes use of the fact that the distance to an object  $D_A$  is the ratio between its physical size and the observed angular size. The dust emission in AGNs, however, does not come from a region of fixed size but from a range of radii contributing to any given observed band. Here we focus on the  $K$ -band emission for the hottest dust around an AGN. As we previously showed using infrared interferometric data<sup>18,21,31</sup>, the radius-dependent brightness distribution  $F(r)$  in any infrared band can be approximated by a power law

$$F(r) \propto \int Q_{\text{abs},\nu} B_\nu(T(r)) \left(\frac{r}{r_{\text{in}}}\right)^{\alpha'} dv$$

where  $B_\nu(T(r))$  is the frequency-dependent Planck function for temperature  $T(r)$  at radius  $r$ , and  $Q_{\text{abs},\nu}$  is the absorption efficiency of the dust. The frequency integration can be approximated by a power law as  $\int Q_{\text{abs},\nu} B_\nu(T) dv \propto T^{4+\gamma}$  (ref. 32). The power-law index  $\gamma$  describes the change of absorption efficiency in the infrared with respect to the optical. For black-body radiation,  $Q_{\text{abs},\nu} = 1$  and  $\gamma = 0$ , while typical astronomical dust has  $\gamma \approx 1.6$ – $1.8$  (ref. 33). Therefore, using the equation of local thermal equilibrium, the emission from radius  $r$  can be expressed by a power law<sup>17</sup>

$$F(r) = F(r_{\text{in}}) \left(\frac{r}{r_{\text{in}}}\right)^{\alpha' - 2/(4+\gamma)} = F(r_{\text{in}}) \left(\frac{r}{r_{\text{in}}}\right)^\alpha \quad (1)$$

where  $F(r_{\text{in}})$  is the emission from the innermost radius  $r_{\text{in}} = r(T_{\text{sub}})$ , where the dust temperature reaches the sublimation temperature  $T_{\text{sub}}$ . Equation (1) is used to model the observed light curves and interferometry (see below). The dust opacity of the emitting medium is thus implicitly accounted for because  $\gamma$  is included in  $\alpha = \alpha' - 2/(4 + \gamma)$ , which is directly constrained by observations. Therefore, we do not need to assume any particular dust composition, but instead solve self-consistently for the effect of dust absorption efficiencies.

The rest-frame light-travel time  $\tau$  from the AGN to radius  $r$  can be expressed as  $\tau = r/c$ , and so we can rewrite equation (1) as

$$F(\tau) = F(\tau_{\text{in}}) \left(\frac{\tau}{\tau_{\text{in}}}\right)^\alpha \quad (2)$$

Equivalently, the observed angular size  $\rho$  is related to  $r$  by  $\rho = r/D_A$  (for small  $\rho$ ), such that equation (1) can be written as

$$F(\rho) = F(\rho_{\text{in}}) \left(\frac{\rho}{\rho_{\text{in}}}\right)^\alpha \quad (3)$$

To measure the angular-diameter distance  $D_A$  to the AGN, we have to determine a time lag and an angular size that are representative of the brightness distribution with power-law index  $\alpha$ . Conveniently, we choose values of the scaling time lag  $\tau_{\text{in}}$  and  $\rho_{\text{in}}$  that correspond to the inner size of the emission region. The power-law index  $\alpha$  may be constrained from both interferometry and reverberation measurements. In practice, we do not cover enough baseline lengths with the available interferometry, and so we use the constraint on  $\alpha$  from fitting the light curves to determine  $\rho_{\text{in}}$  (see below).

The absolute values of both scaling sizes  $\tau_{\text{in}}$  and  $\rho_{\text{in}}$  depend on the choice of  $T_{\text{sub}}$ . However, according to equations (2) and (3), both  $T$  dependences are exactly the same. Therefore, the ratio of  $\tau_{\text{in}}$  and  $\rho_{\text{in}}$  is independent of  $T$ . Nevertheless, we sample  $T_{\text{sub}}$  from a normal distribution with mean of 1,400 K and a standard deviation of 100 K. This choice is based on our previous work, where we were simultaneously fitting the near-infrared spectral energy distribution and interferometry of NGC 4151 by means of a power-law brightness model<sup>18</sup>. We also tested and confirmed that the distance measurement is indeed not dependent on temperature. Extended Data Fig. 1 shows the  $D_A$ – $T_{\text{sub}}$  plane of our 1,250 samples. The Spearman correlation coefficient of  $0.01 \pm 0.03$  is very close to zero, implying that the distribution is consistent with being drawn from an uncorrelated parent distribution.

**Data selection and AGN variability.** NGC 4151 was extensively monitored in the  $V$  and  $K$  bands using the MAGNUM telescope in the period between 2001 and 2006<sup>19</sup>. In 2003, NGC 4151 became the first AGN to be spatially resolved with infrared interferometry using the Keck interferometer<sup>11</sup>. Further Keck interferometry was done in 2009, 2010 and 2011<sup>12,14</sup>.

Changes in the luminosity of the putative accretion disk might influence the size of the hot-dust region via increased or suppressed sublimation. It has been demonstrated, however, that the  $V$ -to- $K$  time lag in NGC 4151 between 2001 and 2006 did not vary significantly despite a peak-to-valley change in luminosity of a factor of  $\sim 20$  in the  $V$  band, which could have changed the radius by a factor of 4–5 (ref. 17). Evidence has been found<sup>16</sup> that any change in the size of the hot-dust emitting region in NGC 4151 requires much stronger variability in terms of luminosity and

has to be sustained for some time. Furthermore, structural changes appear to be delayed on timescales  $\sim 40$  times longer than the time lag<sup>16</sup> ( $\sim 5$  yr). On the basis of separate modelling of the light curve and interferometry, we previously concluded that the inner radius remained unchanged within measurement uncertainties between 2003 and 2010<sup>16,17</sup>. Therefore, the six independent  $K$ -band interferometry data sets from 2003, 2009 and 2010 can be considered contemporaneous with the photometric monitoring and we include them in our analysis.

**Inclination and orientation of the dusty disk.** The model that is used to recover the time lag  $\tau_{\text{in}}$  and angular size  $\rho_{\text{in}}$  of the inner radius of the  $K$ -band brightness distribution accounts for the geometry of the emitting region in terms of a (projected) disk configuration. We showed previously that it is a simplified, yet accurate, representation of the direct (unobscured) hot-dust emission of more complex clumpy or smooth torus models<sup>31</sup>.

The position angle of the AGN system/polar axis (the direction of the minor axis of the projected ellipse) has been inferred from kinematic modelling of emission lines and optical polarimetry (see Extended Data Table 1 for a compilation of data). The various constraints originate from different spatial scales: optical polarization in this type 1 AGN is a result of scattering of the putative accretion disk emission by gas clouds on the scale of the broad-line region, which is about a factor of four smaller than the region of hot-dust emission. These data indicate an orientation approximately towards position angle  $90^\circ$  (refs 25, 34). The outflow kinematics of the narrow-emission region on arcsecond scales point approximately towards position angle  $35^\circ$  (ref. 23) or  $60^\circ$  (ref. 24), with the two different values presumably originating from different modelling approaches. Although the smallest spatial resolutions obtained by polarimetry may arguably best trace the orientation of the AGN, we chose a prior on the position angle of  $75^\circ$  and sample from a normal distribution with a standard deviation of  $15^\circ$  to reflect the range of inferred directions. It is important to note that with future multi-baseline infrared interferometry, both inclination and position angle will be self-consistently inferred from the data without the need for extra information.

Priors for the inclination of the disk come from the kinematic modelling of the emission lines in the outflow cone<sup>23,24</sup>. Despite the differences in position angle from the different modelling approaches, the inclination of the system has been consistently found to be  $45^\circ$ , with varying degrees of uncertainty. Accordingly, we sample inclinations from a normal distribution with a mean value of  $45^\circ$  and a standard deviation of  $10^\circ$ .

**Modelling of the data.**  $V$ - and  $K$ -band light curves. In a first step, the  $V$ -band light curve was resampled to obtain uniform coverage without seasonal gaps. The gaps were filled using a standard stochastic interpolation technique that makes use of the AGN's known variability pattern via the structure function<sup>15,35</sup>. The resampled  $V$ -band light curve was then used as the AGN variability pattern and put into a simplified radiative transfer model of a dust disk<sup>17</sup> to predict a model  $K$ -band light curve given  $\tau_{\text{in}}$ , the power-law index  $\alpha$  of the projected dust (brightness) distribution, the energy conversion efficiency  $\omega_{\text{eff}}$ , the sublimation temperature  $T_{\text{sub}}$  of the dust, and the inclination  $i$  of the disk. Here  $\omega_{\text{eff}}$  represents the fraction of  $K$ -band light that reacts to the variability of the  $V$  band<sup>17</sup>. In the framework of this study, it can be considered a scaling factor of the amplitudes that does not have any influence on the time delay or shape of the variability pattern. As an important step in the process, we base our modelling on the relative light curve  $g_i(t) = f_i(t)/\langle f_i(t) \rangle - 1$  ( $i = V, K$ ) rather than the light curve  $f_i(t)$  to remove any dependencies on the dust covering factor. Here  $\langle f_i(t) \rangle$  is the mean flux of the corresponding band over the entire monitoring period.

To obtain the best representation of the resampled light curve, we implemented a fitting scheme based on the IDL MPFIT fitting package<sup>36</sup>. To do so, the  $K$ -band light curve model fluxes were extracted at the observed epochs. These model  $K$ -band fluxes were compared with the observed  $K$ -band fluxes, and the squared residuals were minimized by varying  $\tau_{\text{in}}$ ,  $\alpha$  and  $\omega_{\text{eff}}$ . The fitting scheme was repeated for 1,250 randomly resampled  $V$ -band light curves to properly account for the uncertainties due to the finite sampling. In this process,  $T_{\text{sub}}$  and  $i$  were treated as fixed parameters rather than as actual model parameters because the light curves do not constrain them. Instead we randomly drew a value from the prior distributions of  $T_{\text{sub}}$  and  $i$  for each resampled light curve that was fitted. This accounts for the systematic uncertainty in these parameters.

Extended Data Fig. 2 shows the two-dimensional distribution of fitted  $\alpha$  and  $\tau_{\text{in}}$  values. The fully marginalized mean values and 68% confidence levels of these distributions are determined to be  $\tau_{\text{in}} = 36^{+9}_{-7}$  d and  $\alpha = -1.7^{+1.2}_{-1.2}$ . Similarly, we found an efficiency factor of  $\omega_{\text{eff}} = 0.46^{+0.06}_{-0.07}$ . These values are consistent with our previously published results<sup>17</sup>.

$K$ -band interferometry. The light-curve resampling and modelling provides us with 1,250 sets of parameters ( $\tau_{\text{in},j}$ ,  $\alpha_j$ ,  $T_{\text{sub},j}$ ,  $i_j$ ). As shown in Fig. 2, the key element in obtaining a precise angular distance is to determine both time lag and infrared interferometry size using the same set of parameters that define the brightness distribution of the object, in particular  $\alpha$ . This parameter is correlated with both  $\tau_{\text{in}}$

and  $\rho_{\text{in}}$ . Although the  $\alpha$ -dependence contributes a high uncertainty to the constraints on  $\tau_{\text{in}}$  and  $\rho_{\text{in}}$  individually, it cancels as a source of uncertainty in the absolute distance, that is, the ratio between both parameters, when determining  $\tau_{\text{in}}$  and  $\rho_{\text{in}}$  self-consistently given the inferred  $\alpha$ .

From  $\alpha_j$ ,  $T_{\text{sub}j}$  and  $i_j$ , we simulated model images of the  $K$ -band emission and fitted the six observed squared visibilities with an angular size  $\rho_{\text{in}}$  of the inner brightness distribution. This conversion from visibility to size depends on the orientation of the emitting disk because two-telescope long-baseline interferometry provides spatial information only along a specific position angle. Therefore, we randomly pick a disk orientation for each individual parameter set on the basis of the prior distribution as constrained by observations (see above). This accounts for the systematic uncertainty in the orientation of the disk. We also correct for the contributions of the host galaxy and the putative accretion disk to the  $K$ -band visibilities<sup>12,14</sup>, and consider the respective uncertainties in our simulations. This additional Monte Carlo sampling was repeated 200 times for each of the 1,250 initial sets of  $(\alpha_j, T_{\text{sub}j}, i_j)$  samples and each of the six independent interferometric measurements.

**Error budget and potential sources of systematic uncertainty.** The geometric distance measurement is based on a power-law parameterization for the brightness distribution in the  $K$  band. Therefore, the uncertainties reflect the probability distribution given the use of this model of 1,250 Monte Carlo samples to recover  $\tau_{\text{in}}$  and  $\alpha$  from the light curve and additional sampling to recover  $\rho_{\text{in}}$  from the interferometric data. It accounts for uncertainties in the geometric parameters (disk inclination and position angle) as well as the statistical errors of the six interferometric observations and the uncertainties in their correction for host and putative accretion disk contributions as far as they are constrained by these data. The observations do not allow us to distinguish between different parameterizations of the brightness distribution, which is an unknown uncertainty at this time. However, this parameterization was successful in simultaneously reproducing near- and mid-infrared photometry and resolved interferometry of NGC 4151<sup>18</sup>, and therefore seems a justified choice.

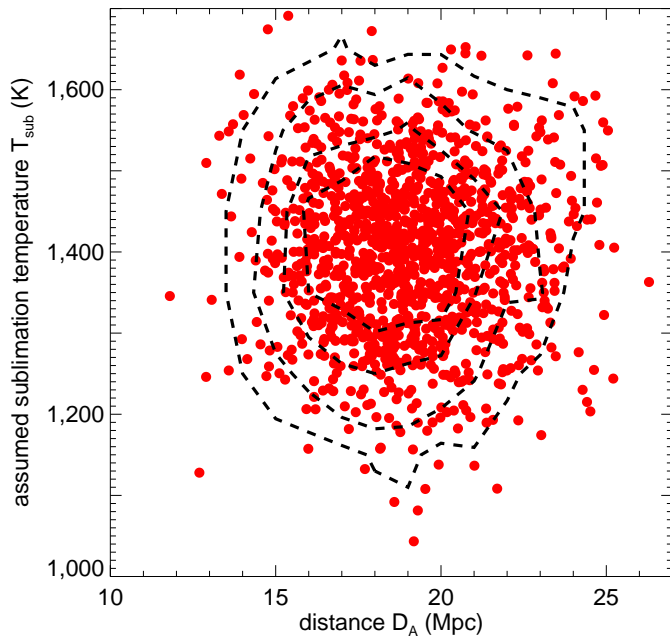
The error in the distance results from a combination of correlated and uncorrelated uncertainties in determining the reference time lag  $\tau_{\text{in}}$ , the reference angular size  $\rho_{\text{in}}$  and the brightness distribution power-law index  $\alpha$ . In Extended Data Fig. 2, we show the distribution of  $\tau_{\text{in}}$  and  $\alpha$  values obtained from fitting the 1,250 random representations of the finite-sampled  $V$ -band light curve given the inclination and  $T_{\text{sub}}$  values extracted from the distributions discussed previously. The total scatter is dominated by the uncertainty in defining the 'true' light curve from the limited number of epochs, with only a small contribution from the sampled range of inclinations. The relative contribution of this fitting to the total distance uncertainty can be estimated from the relative width of the distribution in  $\tau_{\text{in}}$  given  $\alpha$ , and is approximately 6–7% (68% confidence level). Extended Data Fig. 3 shows the distribution of  $\rho_{\text{in}}$  for the 1,250 fitted  $\alpha$  values, inclinations and sublimation temperatures given the six interferometric observations. The grey error bars represent the additional error in  $\rho_{\text{in}}$  from the uncertainty in position angle and in removing the host and putative accretion disk contributions, based on additional sampling of the

interferometric data (see above). As before, we can estimate the relative contribution from  $\rho_{\text{in}}$  from a combination of the scatter of the data points and the individual uncertainties, and find it to be approximately 12% (68% confidence level). This combines to a total error in the distance of about 13.5% as obtained from the probability distribution function of  $D_A$  shown in Fig. 2.

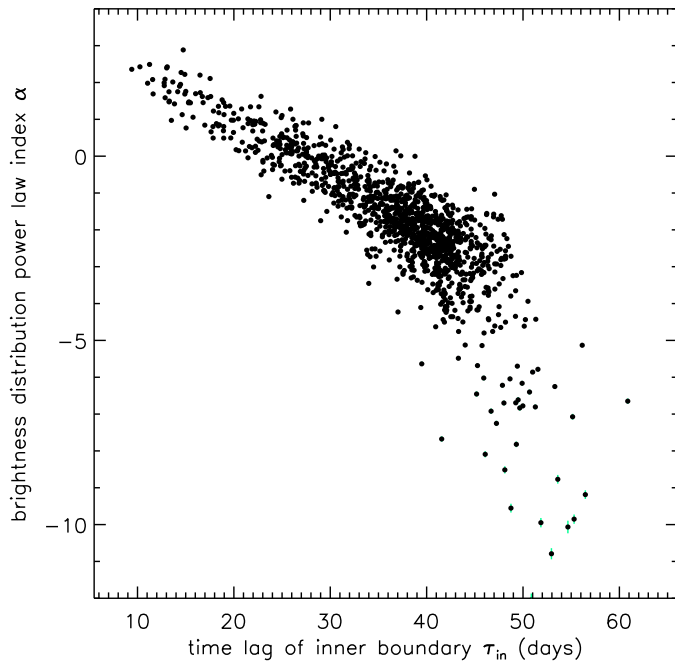
The major sources of systematic uncertainty are the object's inclination and orientation. The prior distributions of  $i$  and the disk symmetry axis orientation are the dominant factors that contribute to the width of the  $\tau$ - $\rho$  correlation. The reason for this is that although the disk orientation influences the conversion of interferometric visibility to de-projected size, it does not have any influence on the time lag signal. The inclination, however, affects both the interferometry and the reverberation signal. In interferometry, it causes a projection effect that decreases the observed size by approximately a factor of  $\cos(i)\sin(\theta)$ , where  $\theta$  is the position angle offset from the disk symmetry axis. For reverberation mapping, however, it only broadens or smooths the time lag signal symmetrically around the mean without a significant shift in  $\tau$ .

Although the dust covering factor cancels out when modelling relative light curves<sup>17</sup>, we implicitly assume that the covering factor in the  $K$  band is small. In the present model, the brightness distribution is a projected disk and, thus, geometrically thin. This simplifies the convolution of the light curves with the transfer function to a two-dimensional problem. If there were a significant amount of emission coming from material highly elevated above the disk, then we would obtain additional contributions to the transfer from the three-dimensional space. Whether the presence of such emission would bias the results towards longer or shorter lags or a more compact or more shallow brightness distribution depends on the exact shape of the inner sublimation zone, which is unconstrained as of now. However, our assumption of a small covering factor is justified by the observed  $K$ -band covering factor of  $c_K \approx 0.2$  as estimated from the mean fluxes of the  $V$ - and  $K$ -band light curves.

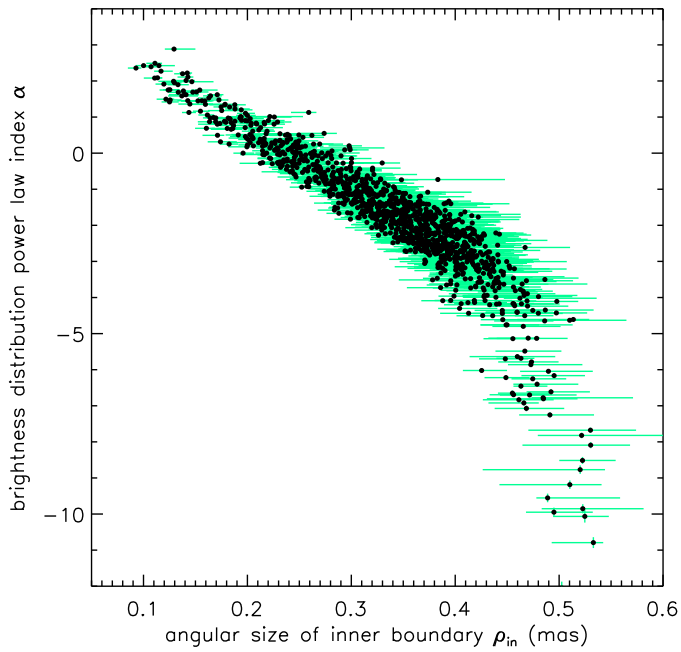
31. Höning, S. F. & Kishimoto, M. The dusty heart of nearby active galaxies. II. From clumpy torus models to physical properties of dust around AGN. *Astron. Astrophys.* **523**, A27 (2010).
32. Barvainis, R. Hot dust and the near-infrared bump in the continuum spectra of quasars and active galactic nuclei. *Astrophys. J.* **320**, 537–544 (1987).
33. Mor, R. & Netzer, H. Hot graphite dust and the infrared spectral energy distribution of active galactic nuclei. *Mon. Not. R. Astron. Soc.* **420**, 526–541 (2012).
34. Merkulova, N. I. & Shakhovskoy, N. M. UBVRl linear polarimetry of the nucleus of the Seyfert galaxy NGC 4151 at maximum and minimum light. *ASP Conf. Ser.* **360**, 65–68 (2006).
35. Peterson, B. M. *et al.* On uncertainties in cross-correlation lags and the reality of wavelength-dependent continuum lags in active galactic nuclei. *Publ. Astron. Soc. Pacif.* **110**, 660–670 (1998).
36. Markwardt, C. B. Non-linear least squares fitting in IDL with MPFIT. *ASP Conf. Ser.* **411**, 251–254 (2009).



**Extended Data Figure 1 | Dependence of the measured angular-diameter distance  $D_A$  on the dust sublimation temperature  $T_{\text{sub}}$ .** The red circles represent the distribution of sublimation temperatures in the 1,250 Monte Carlo runs used to model the light curve. Overplotted are dashed contours at 5%, 15%, 33% and 50% peak density. The distribution of  $D_A$  is consistent with being independent of  $T_{\text{sub}}$ , illustrating that the distance determination is insensitive to the detailed dust properties.



**Extended Data Figure 2 | Dependence of the time lag  $\tau_{\text{in}}$  of the inner boundary on the brightness distribution power-law index  $\alpha$ .** The black circles represent the fitted  $\tau_{\text{in}}$  and  $\alpha$  values for each of the 1,250 Monte Carlo representations of the V-band light curves given the inclination and sublimation temperature distributions (68% fitting error levels, mostly smaller than the symbol size).



**Extended Data Figure 3 | Dependence of the angular size  $\rho_{\text{in}}$  of the inner boundary on the brightness distribution power-law index  $\alpha$ .** The black circles represent the distribution of  $\rho_{\text{in}}$  determined from the six interferometric data points for a given  $\alpha$  value, sublimation temperature and inclination for each of the 1,250 Monte Carlo representations of the V-band light curve. The cyan error bars represent the additional uncertainties (68% confidence levels) from the combined statistical errors of the observations, the position angle of the emitting disk and the corrections for host and putative accretion disk contributions.

**Extended Data Table 1 | Constraints on the inclination and position angle of the AGN structure from various observations**

<i>method</i>	<i>inclination</i>	<i>position angle</i>	<i>approx. scale</i>	<i>reference</i>	<i>distance</i>
optical continuum	...	91°	< 0.''01	continuum near H $\alpha$ line <sup>25</sup>	20.4 $\pm$ 1.6 Mpc
polarimetry	...	92° $\pm$ 2°	< 0.''01	<i>UBVRI</i> polarimetry <sup>34</sup>	20.5 $\pm$ 1.6 Mpc
kinematic modeling	45° $\pm$ 5°	35°	> 1''	bicone <sup>23</sup>	15.7 $\pm$ 2.4 Mpc
of emission lines	45°	60°	< 2''	bicone <sup>24</sup>	18.0 $\pm$ 1.8 Mpc
<b>combined inference</b>	<b>45° <math>\pm</math> 10°</b>	<b>75° <math>\pm</math> 15°</b>	...	...	<b>19.0<sup>+2.4</sup><sub>-2.6</sub> Mpc</b>

The inferred distance for each individual observation does not include any uncertainties in the position angles and assumes an inclination of 45°  $\pm$  10°.